Nonresonant optical tagging and "monopolar" transport in negative-ion plasmas

R. A. Stern,
Department of Astrophysical, Planetary, and Atmospheric Sciences and Department of Physics, University of Colorado, Boulder, Colorado 80309

P. Devynck, M. Bacal, P. Berlemont, and F. Hillion
Laboratoire de Physique des Milieux Ionisés, Laboratoire du Centre National de la Recherche, Ecole Polytechnique, Palaiseau, France
(Received 25 April 1989; revised manuscript received 4 December 1989)

A diagnostic method has been devised and used to measure local transport velocities of negative hydrogen ions (H^-) within a gas-discharge source chamber. The method is based on laser-pulse photodetachment of negative ions, inducing local changes in the electron and ion densities, whose space and time evolution are traced in detail by means of laser pulses and probes. The technique, which has general applicability, can be used in plasmas where conventional probe or spectroscopic methods are not practicable. A new plasma transport process—monopolar drift—in which particles with the *same* charge counterflow—is identified by means of this technique. This process can be dominant in multispecies plasmas, i.e., those containing negative as well as positive ions. A kinetic analysis of the plasma evolution in space-time, following localized photodetachment of the negative ions, is presented. The results are compared with the first experimental data obtained on H^-, demonstrating the principal modes of the diagnostic technique. The consistency between analysis and experiments indicates that the method is generally useful, and principles for its extension are laid out.

I. INTRODUCTION

Plasma ion diagnositics are of central importance in several fields including basic plasma physics, fusion, and particle beams. Current techniques—probes and spectroscopy—have limited applicability in broad categories of plasmas, such as multispecies plasmas containing both positive and negative ions as well as electrons, or plasmas with ions which possess no accessible excited bound states. A notable example of this class is negative hydrogen (H^-), a plasma constituent that controls radiation transport and opacity in the atmospheres of the sun and similar stars. It is also technologically important in the production of energetic neutral beams for heating and diagnostics in fusion plasmas.[1] We have developed a class of basic and generally applicable diagnostic techniques suitable for such cases, and used them to measure and characterize the H^- transport velocities within a volume source. Using these techniques, we have found and described theoretically as well as experimentally a basic transport process that can occur in multispecies plasmas: "monopolar" drift, in which particles with *the same charge* preserve local neutrality by *counterflowing* (in contrast with the well-known ambipolar drift, which involves oppositely charged species flowing in the same direction). This process, for instance, governs the interaction between adjacent plasmas which interact without the application of an initial perturbation in the electric field or net charge density, due only to differing "composition," i.e., charged-particle fractional densities. In our example, monopolar drift causes a nearly two order of magnitude decrease in the electron transport speeds below thermal values expected in such media.

A simple way to measure transport is to render the medium inhomogeneous in a controlled manner, and analyze the space-time details of its return to equilibrium. The problems involved are (i) to construct a model that describes the plasma evolution in response to the perturbation, in terms of the transport parameters; and (ii) to devise methods for measuring the recovery in plasma properties, with sufficient resolution. The fit of model to measurement is then used to unfold actual values of the transport parameters. Correspondingly, this communication describes (i) a formal kinetic analysis of the plasma density evolution following strong localized changes in the negative ion and electron densities caused by laser photodetachment, including the self-consistent electric field induced by the perturbation; and (ii) the measurement method, a generalized version of optical tagging.[2] These are applied to plasmas containing H^-. Preliminary experimental data obtained using several variants of the technique are analyzed in terms of the model, to demonstrate feasibility and point out future directions.

The organization of the paper is the following. Section II presents the physics underlying optical tagging in the generalized sense. Sections III and IV detail the experimental configuration and the data acquisition schemes ("dark" and "bright" signal modes) used in the measurements. The physical principles and procedure for deducing transport properties from tagging data are sketched out in Sec. V, while Sec. VI presents a formal kinetic analysis of the strongly nonuniform initial-value problem in a three-species positive-negative ion plasma, carried out to first order in the potential, in a collisionless plasma subject to photodetachment of the negative ions. The final sections compare analysis with data obtained in H^- plasmas, and summarize the results. The conclusions are that nonresonant optical tagging can be an effective diagnostic in several modes, and that transport governed by the negative ions, with a secondary role assumed by the electrons and positive ions, may be dominant in strongly nonuniform multispecies plasmas.

II. DIAGNOSTIC CONCEPTS

The following physical principles underlie our measurement method, which is an application of optical tagging,[2] a set of diagnostic techniques specifically developed to characterize transport. In tagging, optical pumping is used to alter the relative densities of two long-lived, radiatively connected quantum states of a given particle, by means of a "pump" laser beam switched on at the position and instant of interest—the "source" point. The particle migration away from the source is then traced in space and time, to a "field" point, using a "search" beam-detector combination, which is sensitive to changes in the density of *either* long-lived quantum state (the bright and dark, or Kastler and Dehmelt schemes). As with time-of-flight techniques, tagging employs the space-time variation in particle density to determine transport velocities, through the connection between density, temperature, and velocity imposed by conservation laws.

To date, tagging has been applied only to particles in which the quantum states involved are *both bound levels.* Since optical pumping cross sections are proportional to the overlap product of absorption linewidth and laser spectral width, the narrow resonant transitions involved require pump, search, and detector functions to consist of narrow-band, tunable optical radiation—a serious restriction. The novel feature of the present method is its extension to particles which have *no bound excited* states; i.e., one of the states lies in the continuum. In addition to enlarging the range of plasmas to which the method can be applied, this obviates the need for narrow-band tunable radiation, enabling a range of powerful, broadband lasers or incoherent light sources to be brought to bear.

The technique was applied to an H^- volume source.[3] These are hot-cathode gas discharges in which H^- is generated primarily by dissociative electron attachment to excited vibrational states of H_2.[4] Typically of negative-ion plasmas, the presence of electrons as well as the quantum-state structure of H^- preclude the direct use of probe, laser,[5] or classical spectroscopic techniques. We choose instead to tag the negative ion by pumping it from the ground state into the continuum using laser-induced photodetachment.[6,7] A broad, continuous range of wavelengths from the near-ir to the uv can be used to this purpose, with cross sections as large as 10^{-17} cm^2. In this tagging scheme, the final state (after pumping), which is long lived because of the low volume recombination and attachment rates, now consists of *two particles*—an electron and an atom—*either* of which may be traced in space-time by the search function.

In our experiment, the choice of pump laser wavelength results in final states with the free atom generated in its ground level. Interrogating this atom would require vacuum-uv as search radiation. To avoid the technical complications associated with this, the search function in the *bright* signal mode is performed directly on the free electron using positively biased Langmuir probes,[7] axially and radially movable across the source. For the *dark* signal mode, the beam searching for the depleted H^- density is a second Nd:YAG pulse (where YAG is yttrium aluminum garnet) delayed in time from the pump, and the detection is carried out on the final-state photoelectron using probes, as above. We note that alternatives that may be considered would use (i) tunable dye-laser radiation in the visible tripled or quadrupled to generate Lyman lines, or else (ii) a high-energy photon, or a multiphoton scheme, for the pump beam, leaving the final atom in an excited state directly accessible to interrogation by conventional optical methods, e.g., laser-induced fluorescence.[5]

III. EXPERIMENTAL CONFIGURATION

Figure 1 presents a diagram of the cylindrical hybrid multipole source.[3] This is a cylindrical hot-filament gas discharge operated in hydrogen, 25 cm in diameter and 26 cm high, with a permanent magnet array near the chamber walls to limit plasma losses. Typical operating conditions are 5 A discharge current at 50 V and 3 mTorr, unless otherwise indicated. The density range was 10^{10}–10^{11} cm^{-3}, with 0.5-eV thermal energy for the electrons, Debye lengths λ_D ranging from 10^{-2} to 10^{-3} cm, and up to 12% of the negative charge present as H^-. The electron properties are determined from Langmuir probe traces; the H^- density is obtained from the ratio of the peak of the probe photodetachment signal to the probe dc signal, a technique described in Ref. 7. It makes use of the fact that the dc signal is proportional to the electron density, while the peak is proportional to the H^- density. Under our conditions the mean free path of the electrons is comparable to the chamber dimensions, so that the pulse of photodetached electrons can be detected by a remotely located, nonperturbing electrode. The principal collision mechanism for H^- at these conditions (low pressure, discharge current and electron temperature) is with H_2, for which[8] the product $\sigma v = 2.5\times10^{-9}$ cm^3 sec^{-1}. We have typically densities of H with values $N \approx 9\times10^{13}$ cm^{-3}, so that the collision time $(N\sigma v)^{-1}$ is about 5 μs. Adding corrections for collisions with $H_{2,3}^+$ decreases this to 4 μs (longer than the times we will be

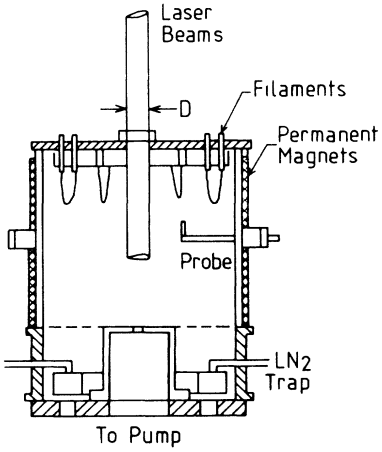

FIG. 1. Diagram of the volume H^- hybrid multipole source.

concerned with, $t < 1$ μs), so that a collisionless approximation is appropriate in this regime. At typical ion temperatures of 0.2 eV, the H^- mean free path is nearly 2 cm, an order of magnitude larger than the test volume radii ($R = 0.2$ cm), where the best fit is obtained. No evidence of plasma destabilization by the probe is observed.[1,7]

Figure 2 describes a typical diagnostic geometry. Laser light, limited by a circular baffle to a beam of diameter $D = 1.2$ cm or less, is admitted into a source through a window in the center of the chamber end flange. The laser beam axis is aligned with the chamber axis. The particle density is low enough to ensure the plasma is optically thin. The pump and search lasers used are Nd:YAG lasers at 1.06 mm, typically 15-ns duration and a few hundred mJ in pulse energy, synchronized to produce pulses with < ns jitter and operated with controlled delays Δt between pulses, ranging from 10 to 10 000 ns. Since the photodetachment cross section at this wavelength is near its peak, a photon pulse flux of order 10^{17} cm^{-2} (tens of mJ/cm^2) sufficies to depopulate the H^- ground state entirely. The technique is selective in H_2 discharges, since only H^-, of all species present, will be photodetached with sufficient cross section at these photon energies.[7] For Nd:YAG pulses, the free electrons are generated with energies at most equal to 0.45 eV, i.e., very near the background electron temperature.

A Langmuir probe is positioned at the midplane of the chamber, and can be moved across the plane. The probe, typically a tungsten wire 0.5 mm in diameter, 1.5 cm long parallel to the beam axis, is biased to 20 V, much above the plasma potential (normally 2V), and collects dominantly an electron current. The photoelectron burst released in either mode by the laser pulse is discriminated from the background (dc) electron current to the probe through the use of capacitive coupling.

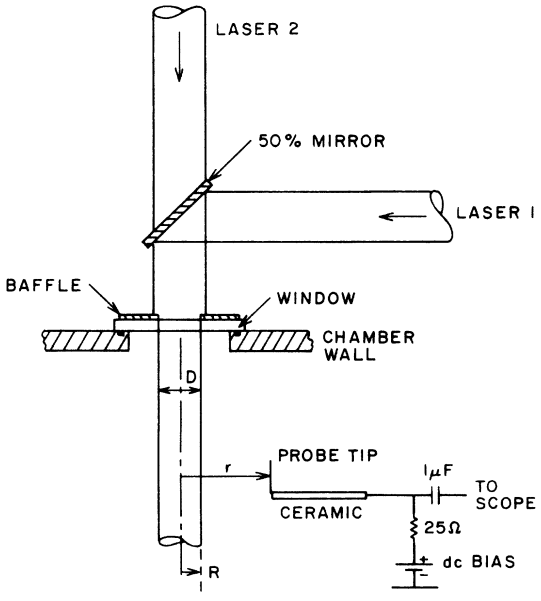

FIG. 2. Schematic of diagnostic instrumentation and geometry.

IV. DATA ACQUISITION MODES

We present first experimental results obtained using the dark-signal mode, which yields a direct observation of H^- transport. In our scheme, the pump beam pulse initially depletes all the negative-ion population within the test volume—the cylinder whose diameter equals the beam diameter D. It is followed by a search laser pulse, whose beam is aligned (coaxial) with the pump, and switched on at a delayed time Δt. The search pulse will photodetach those H^- ions which have flowed into the test volume during the interval Δt, from the surrounding region $r > R$ (where r is the radial distance from the center of the beam and $R = D/2$). Since one electron is released from each H^- ion (with laser intensities above saturation), an excess of electrons is produced, whose density Δn_e equals the H^- density $n_-(r, \Delta t)$ at that time. A Langmuir probe located at r and biased positively to collect electrons will therefore register a rapid signal rise in coincidence with the search pulse. The magnitude of this peak is proportional to $\Delta n_e = n_-(r, \Delta t)$. This quantity increases with Δt, as more H^- ions have had time to flow into the test volume, and eventually saturates.

A typical probe signal obtained from a single laser pulse is shown in Fig. 3 (upper trace). It starts off with a

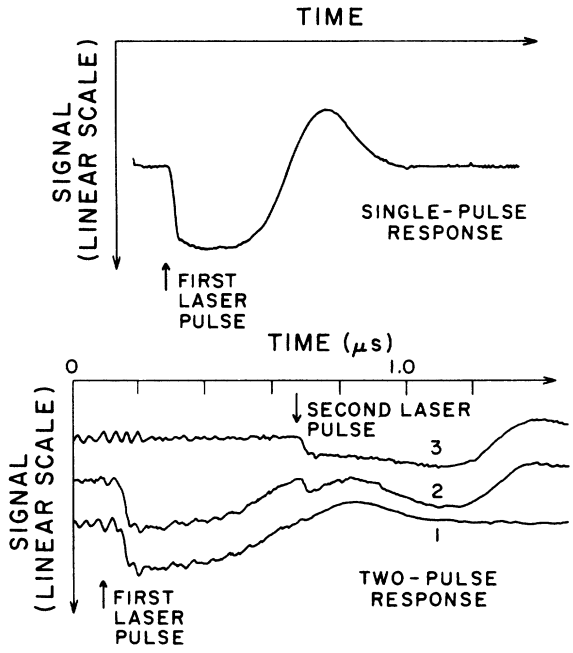

FIG. 3. Upper trace: typical probe current pulse following a single laser photodetachment pulse at $r = 0$. Abscissa: time, linear scale. Ordinate: probe electron current, linear scale (more light = signal down). Lower traces: typical probe current pulses used in "dark" signal mode: 1, pump pulse only; 2, pump pulse followed by delayed search pulse; 3, computer-calculated difference between 1 and 2, showing negative-ion density recovery at time of search pulse. For convenience, the baselines are displaced vertically. Abscissa: time, 200 ns/division. Ordinate: probe electron current, linear scale (more light = signal down). Arrows indicate pump ($t = 0$) and search laser switch-on times.

sharp initial voltage drop, representing the immediate increase in probe electron current, due to photodetachment. It is followed by a slower rise to a peak, and thereafter the signal falls off gradually, eventually returning to the baseline and crossing it, i.e., exhibiting an overshot which corresponds to a decrease in the electron density below the background value. These features will be discussed in more detail below.

In the dark mode, two probe signals are acquired within a short delay, and therefore overlap in time to varying extents. A typical sequence of such signals is illustrated in the lower traces of Fig. 3. Trace 1 shows the probe signal from a single pump pulse. Trace 2 shows the probe signal from a sequence of probe plus search pulses, delayed by $\Delta t = 250$ ns. Using digital data acquisition and computer processing, trace 1 is subtracted out from trace 2, exhibiting the net search signal (trace 3) and its initial drop, whose magnitude represents the photodetached excess electron density at $\Delta t = 250$ ns. Carrying out measurements of this type over a range of Δt, one obtains the typical data plotted in Fig. 4. Here the probe is at the center of the beam $r = 0$, so that the experiment traces the density function n_- $(r = 0,\ t = \Delta t)$, the temporal recovery in H^- due to transport from the surrounding volume $r > R$.

Since the background probe signal (dc) is proportional to the (measured) initial electron density, and the probe response is linear, it follows that the absolute value of n_- can be obtained from the ratio of the initial peak to the dc probe currents. This has long been a standard method for measuring H^- *densities*, and was used to establish the values of 12% for the ratio of H^- to total negative charge density. Microsecond delays to reestablish steady state were observed and attributed to the *ambipolar* potential in an internal communication[8] as early as 1978, but no study of the space-time evolution of the density nor analysis of the process to extract transport information ensued.

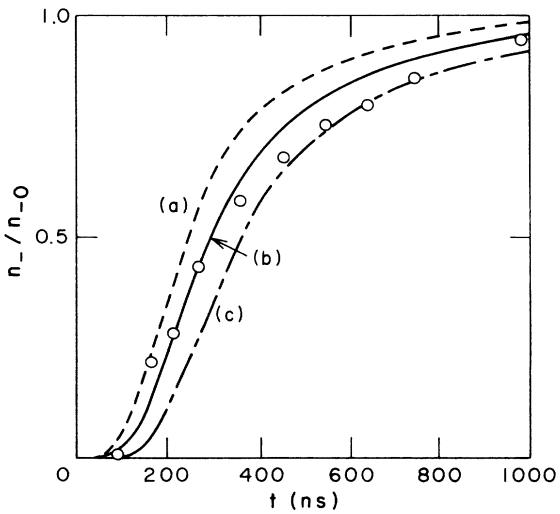

FIG. 4. Recovery of H^- density at $r = 0$ for $R = 0.2$ cm, and data fits using the ballistic approximation, Eq. (11). Parameter values R/v_{th-} are (a) 2×10^{-7} s, (b) 2.5×10^{-7} s, (c) 3×10^{-7} s.

V. PHYSICAL PRINCIPLES

Physical principles for unfolding transport properties from such measurements are described below. Note that, since the background plasma was neutral, and the laser photodetachment pulse perturbation produces no net charge, the plasma is *initially stationary and electric-field free* everywhere. This is a relatively unusual initial condition, unlike the common situations in which the plasma is initially rendered non-neutral, or else where the form of the distribution function is initially perturbed, as in current- or drift-destabilized plasmas. Instead, we are dealing with two concentric, equipotential (field-free) neutral plasmas with the same total charge density, stationary (i.e., with no relative fluid speed), and differing only through the relative fractions of negative charge which they contain. Here, therefore, the field is initially zero and grows (weakly) as a result of the strong initial density differences. This is the inverse for instance of plasma echoes—a classical configuration which is generated by applying strong initial potential gradients, which cause a (weak) density perturbation to grow. Thus our treatment will differ in essential aspects from previous analyses.

The "perturbation" that starts the process in our case are the gradients in electron and H^- densities at the interface between the two regions $r > R$ and $r < R$; and the initial driving mechanisms are the thermal, field-free particle velocities of the two negative species. That is, the differences in the densities of negative particles between the two regions begin to smear out due to their kinetic motion across $r = R$. Since the densities and particle velocities differ, their fluxes can be unequal, eventually causing net charge accumulation and thereby the buildup of a self-consistent electric field. This field will tend to reduce the fluxes, may oscillate, and eventually leads to a stationary state. In principle, a complete description of the density evolution for all species can be generated, valid at all points and times, including the late period when the diagnostic-induced self-consistent field has grown to finite size. It is useful from an experimental viewpoint, however, to evaluate the growth of this field and isolate regimes in space-time where its effect is weak or negligible, so that the simplest possible model can be developed to interpret the measured data. This is our procedure here; and the general but elaborate late-time solution will be left for a future article.

VI. ANALYSIS OF PLASMA DYNAMICS

A. General solution

The problem is treated kinetically by the coupled Boltzmann and Poisson equations. We limit ourselves to early times in the evolution, i.e., a period short in comparison with collisional times. The kinetic (Vlasov) equations then have the form

$$\frac{\partial f}{\partial t} + \mathbf{v}\cdot\frac{\partial f}{\partial \mathbf{r}} + \frac{e}{m}\mathbf{E}\cdot\frac{\partial f}{\partial \mathbf{v}} \approx 0 , \tag{1}$$

where $\mathbf{E}$ is the electric field vector, derivable from a scalar potential ϕ. Here $f_{e,-,+}(\mathbf{v},\mathbf{r}t)$ are the Boltzmann ve-

locity distribution functions for the electrons, negative and positive ions, respectively, and e/m is the charge-to-mass ratio for each species. The self-consistent field satisfies the Poisson equation

$$\nabla\cdot\mathbf{E}=-\nabla^2\phi=4\pi\sum_{i=+,-,e}e_i n_i\ , \tag{2}$$

where each density $n_{e,-,+}$ is an integral of the corresponding distribution function $n(\mathbf{r},t)=\int d\mathbf{v}\,f(\mathbf{v},\mathbf{r},t)$. The initial value of the field is zero. Due to the tendency of the plasma to neutralize charge inhomogeneities, the growth of the field will be weak. Therefore, during the early time period, the field-dependent components of f can be neglected in the nonlinear term $\mathbf{E}\cdot\partial f/\partial\mathbf{v}$. A formal solution of Eq. (1) is then

$$f(\mathbf{v},\mathbf{r},t)=f(\mathbf{v},\mathbf{r}',t')|_{t'=0}+\frac{e}{m}\int_0^t dt'\mathbf{E}(\mathbf{r}',t')\frac{\partial f_0(\mathbf{v},\mathbf{r}')}{\partial\mathbf{v}}\ , \tag{3}$$

where

$$\mathbf{r}'=\mathbf{r}+\mathbf{v}(t'-t) \tag{4}$$

is the zeroth-order (field-independent) particle orbit, and

$$f_0(\mathbf{v})=\pi^{-3/2}v_{\rm th}^{-3}e^{-(Vx^2+Vy^2+Vz^2)/v_{\rm th}^2} \tag{5}$$

is the field-independent background velocity distribution function, chosen to be a Maxwellian in this case. The spatial variation in the initial density (piecewise constant), caused by the pump photodetachment pulse, is specified for each species in Sec. VI C below, and in the Appendix.

The lowest-order, approximate solution of the system of Eqs. (1)–(5) for our case is obtained as follows. As shown by the right-hand side (rhs) of Eq. (3), the system contains both ballistic and collective (field-dependent) terms. Because of (i) the *particular initial conditions* of this experiment, which starts out with strong spatial density gradients and *null fields,* and (ii) the very large mass ratio between ions and electrons, the first (ballistic) term on the rhs will be dominant for the massive ions at early times, whereas the second (collective) term will govern the density of the low-mass electrons (due to the evolving self-consistent field). Our approach is therefore to evaluate the ballistic and collective density terms neglecting their coupling at the start (early times), insert them into the Poisson equation, and derive an approximate expression for the evolution of the self-consistent potential [Eq. (16) below].

B. Ballistic terms

We first carry out the integrations that yield the ballistic density components for the species. These are defined from Eq. (3) as

$$n_B\equiv\int d\mathbf{v}[f(\mathbf{v},\mathbf{r}',t')]|_{t'=0}\ . \tag{6}$$

The approximate densities n_B will be reduced to a tabulated function of the arguments for an isotropic plasma with a Maxwellian background distribution function, Eq. (5). Because $\mathbf{r}'$ is a function of $\mathbf{v}$, Eq. (4), the integral can be transformed into an integral over $d\mathbf{r}'$, subject to use of the appropriate Jacobian. It is most convenient to use polar coordinates r',θ',z' and r,θ,z. This yields, after some algebra [see the Appendix, Eqs. (A1)–(A10)]

$$n_B(\mathbf{r},t)=n_B(r,\theta,z,t)=n_0\pi^{-3/2}v_{\rm th}^{-3}\int d\theta'\int\frac{dr'}{t}(r'/t)e^{-[(r\cos\theta-r'\cos\theta')^2+(r\sin\theta-r'\sin\theta')^2]/(v_{\rm th}t)^2}\int\frac{dz'}{t}e^{-(z-z')^2/(v_{\rm th}t)^2}\ . \tag{7}$$

Here n_0 is the magnitude of the initial ($t=0$) density for each species. Since we consider a uniform background for $t<0$, in our geometry the initial density will be piecewise constant. For instance, for the negative ions n_0 is nonzero only for $R_{\rm min}<r'<R_{\rm max}$, $z_l<z'<z_u$, where $R_{\rm min}$ and $R_{\rm max}$ are the inner and outer radii of the cylindrical source region ($R_{\rm min}=R$, laser radius; $R_{\rm max}=$ source radius). Similarly, z_u and z_l are the z coordinates of the top and bottom of the source. The integration limits in Eq. (7) are then $\theta'=0$ and 2π, $r'=R_{\rm max}$ and $R_{\rm min}$, and $z'=z_u$ and z_l. For the other components the corresponding limits are given below in Sec. VI C.

Expanding the exponent in Eq. (7), the angular integral can be carried out (see the Appendix). It yields $2\pi I_0(2rr'/(v_{\rm th}t)^2)$, where I_0 is the Bessel function of the first kind of imaginary argument. Note that the θ dependence of n vanishes, as it should in the cylindrical symmetry of this configuration.

The dz' integral is proportional to the difference between two error functions with arguments $z_u/v_{\rm th}t$ and $-z_l/v_{\rm th}t$, respectively. It turns out that in our experiment the magnitudes of both arguments are $\gg1$. The functions therefore tend to $\pm\pi^{1/2}v_{\rm th}/2$, so that the dz' integral reduces to the constant factor $\pi^{1/2}v_{\rm th}$. The reasons are the following. The measurements are conducted near the middle of the chamber, whose midplane is defined as $z=0$. The limits z_u and z_l are typically $+12$ and -12 cm. For the ions, typical $v_{\rm th}<10^6$ cm s^{-1} and characteristic times are of order 0.5 μs, hence the ratios $z/v_{\rm th}t\cong20$. For the electrons, $v_{\rm th}$ is typically 3×10^7 cm s^{-1}, but characteristic times for ballistic decay turn out to be only of order 20 ns, so that the ratio is approximately the same. The physical significance is that the end boundaries are so remote from the point of measurement, that their influence is negligible in the early phases of the process.

Making use of these intermediate results, Eq. (7) reduces to

$$n_B(r,z=0,t)\cong 2n_0 e^{-(r/v_{\rm th}t)^2} \times \int \frac{dr'}{v_{\rm th}t}\frac{r'}{v_{\rm th}t} e^{-(r'/v_{\rm th}t)^2} I_0(2rr'/(v_{\rm th}t)^2) , \quad (8)$$

where the integration limits are $R_{\rm min}/v_{\rm th}t$ and $R_{\rm max}/v_{\rm th}t$. Finally, we associate the radial integral in Eq. (8) with the well-known operational function $J(x,y)$. This function is defined[9]

$$J(x,y)\equiv 1-2e^{-\rho^2}\int_0^\beta te^{-t^2}I_0(2\rho t)dt , \quad x=\beta^2,\ y=\rho^2 . \quad (9)$$

In our notation, β will take the two values $R_{\rm min}/v_{\rm th}t$ or $R_{\rm max}/v_{\rm th}t$, while $\rho=r/v_{\rm th}t$ only. The function J lies between 0 and 1. Some elementary properties of J include $J(0,y)=1$; $J(\infty,y)=0$; and $J(x,0)=e^{-x}$. Expressing the integral in Eq. (8) in terms of J finally yields the general solution for the ballistic density component

$$n_B(r,z=0,t)/n_0\cong J((R_{\rm min}/v_{\rm th}t)^2,(r/v_{\rm th}t)^2) - J((R_{\rm max}/v_{\rm th}t)^2,(r/v_{\rm th}t)^2) . \quad (10)$$

Here the coefficient n_0 represents the background density.

C. Application to the individual species

We can now apply the preceding, fairly general results to our specific configuration. The negative ions are initially (after the laser pulse) present only within the outer cylindrical region between $R_{\rm min}=R$, the laser radius, and $R_{\rm max}\cong 12$ cm, the chamber wall. Let their thermal velocity be characterized by $v_{\rm th-}$. For early times, $R_{\rm max}/v_{\rm th-}t$ will be 20 or larger, so that the second J in Eq. (10) tends to zero. This leaves for the ballistic limit of the negative-ion density the expression

$$n_{-B}(r,z=0,t)/n_{-0}\cong J((R/v_{\rm th-}t)^2,(r/v_{\rm th-}t)^2) \equiv J_- . \quad (11)$$

It should be observed that this function is independent of the geometric dimensions $R_{\rm max}$ and $z_{l,u}$ of the chamber only because of the large values of the arguments, i.e., the fact that the inner region (laser beam radius) is small, and the measurements are carried out near the midplane of the chamber. For an exact, general solution, the error functions incorporating the z limits, as well as the additional term in J from the $R_{\rm max}$ limit, must be included, as described quantitatively above. Note in Eq. (11) the physically correct results that (i) when $R=0$, n_{-B} will attain its final value instantaneously; (ii) if $R=\infty$, n_{-B} will retain its initial, null value; and (iii) at the center $r=0$, the ballistic negative-ion density has a simple dependence

$$n_{-B}(\mathbf{r}=0,t)=n_{-0}e^{-R^2/(v_{\rm th-}t)^2} . \quad (12)$$

This function starts at zero for $t=0$, increases monotonically, tends to n_{-0} as t approaches infinity, and therefore fits the initial and final conditions for the density within the test region.

For the positive ions, which are not affected by the laser pulse initially, the values of $R_{\rm max}$ and $R_{\rm min}$ are approximately infinity and zero, respectively. Introducing this into Eq. (10) yields the physically expected result for the ballistic density

$$n_{+B}(r,z=0,t)/n_{+0}=1 . \quad (13)$$

For the *excess* electrons in the ballistic limit, on the other hand, the initial condition corresponds to $R_{\rm max}=R$ and $R_{\rm min}=0$, since the excess is confined to the laser beam radius. Introducing these conditions into Eq. (10) yields

$$\Delta n_{eB}(r,z=0,t)/\Delta n_{e0} = 1-J((R/v_{\rm the}t)^2,(r/v_{\rm the}t)^2)\equiv 1-J_e , \quad (14)$$

where $v_{\rm the}$ designates the electron thermal velocity, and Δn_{e0} is the initial *excess* density of electrons (created at time $t=0$), equal to n_{-0}.

The background values are connected as follows. Let the negative ion density be a fraction ϵ of n_{+0}. Then $n_{-0}=\epsilon n_{+0}=\Delta n_{e0}$, so that neutrality requires the background electron density $n_{e0}=(1-\epsilon)n_{+0}$. Combining these results with Eqs. (12)–(14) we find that the net ballistic charge density buildup within $r<R$ reduces to the sum

$$e(n_+-n_--n_e)_B=e\epsilon n_{+0}(J_e-J_-) . \quad (15)$$

This is physically intuitive, since it indicates that the ballistic charge accumulation is linear in the excess density ratio ϵ, and would also vanish if the thermal speeds of electrons and negative ions were identical so that $J_e=J_-$. On the ionic time scale, however, $J_e\approx 1$ and the electron velocity distribution function must be assumed to be in equilibrium with the self-consistent field. That is, we use the quasistatic approximation[10] for the electrons in the Poisson equation. The field-dependent component of n_e is

$$n_{e\phi}\cong n_0\frac{e}{kT_e}\phi ,$$

where n_0 is the background density of the electrons, which must equal n_{+0}. The total electron density is therefore

$$n_e\cong n_{+0}(1+e\phi/kT_e) .$$

Introducing this field-dependent limit for n_e, together with the *ballistic* charge density components of the two ion species, and using the appropriate relations between the background values, into the Poisson equation then yields

$$\Delta^2\phi\cong -4\pi e[n_{+B}-n_{-B}-n_{+0}(1+e\phi/kT_e)] = 4\pi e n_{+0}(\epsilon J_- +e\phi/kT_e) . \quad (16)$$

This equation contains both ballistic and field-dependent (collective) terms. In the limit $\epsilon=0$, e.g., if there were no negative ions present to be detached, Eq. (16) reduces to

the expected equation for the static potential in a "normal" positive ion-electron plasma $\Delta^2\phi=\phi/\lambda_D^2$, where λ_D is the Debye length. Consequently, the potential here depends dominantly on the density and thermal speed of the *negative ions only,* justifying the description of the process as "monopolar." The static screening term, which represents the linear reaction of the plasma background tending to shield out the growing potential perturbation, should also contain a field-dependent contribution from ions in principle. If we limit the application of this approximation to early times on the ionic scale, when the ions inertia dominates, such corrections can be expected to be negligible in comparison with the other terms in the Poisson equation.

D. Field evaluation

Formally, Eq. (16), an inhomogeneous Helmholtz equation, can be solved for ϕ in terms of the given forcing function ϵJ_-. We evaluate instead the magnitude of ϕ, and therefore the size of the field-dependent correction to the negative ion ballistic density, by means of the "plasma approximation." It assumes the static screening is sufficiently effective that, in Eq. (16), the term $\Delta^2\phi$ be negligible in comparison with ϕ/λ_D^2; i.e., the plasma will screen out potential variations over spatial scales larger than the Debye length. The remaining two terms then yield the value of the normalized potential

$$\frac{e}{kT_e}\phi\approx-\epsilon J \ . \tag{17}$$

For our experimental conditions, $\epsilon\leq 0.12$. At the center $r=0$, for instance, $e\phi/kT_e$ has the typical value 0.044 at the e^{-1} folding time $t=(R/v_{\text{th}-})$ of the ballistic evolution. During this period of time therefore, since $e\phi/kT_e\ll 1$, the plasma may be considered to be neutral. Consequently, the positive-ion density may be expected to equal the total negative (electron plus H^-) density.

Because of this low value of the potential, an iteration into the full Vlasov equation may not be necessary at this stage. One can estimate instead the effect which the potential has on the ionic speeds. Consider, for instance, charged particles moving at their characteristic speed, the thermal velocity v_{th}. The effect of the potential is to change this velocity to a value $v_{\text{th}}(\phi)$, where the kinetic energy balance requires

$$[v_{\text{th}}(\phi)^2-v_{\text{th}}^2]/v_{\text{th}}^2=-e\phi/kT \ ,$$

hence

$$v_{\text{th}}(\phi)/v_{\text{th}}\cong 1-e\phi/2kT \ .$$

To apply this formula to negative ions, an estimate of T_- is needed. We use for this purpose the experimentally determined value of $v_{\text{th}-}$, e.g., from Fig. 4. This corresponds to a temperature ratio $T_e/T_-\approx 1$, so that $e\phi/2kT_-=0.022$ at the e^{-1} folding time. It indicates that the potential introduces a correction in the effective $v_{\text{th}-}$ of the negative ions which is typically 2%. Since this is less than the experimental precision, a higher-order calculation would yield no significant corrections. We conclude therefore that the ballistic term n_{-B} is a sufficiently close approximation to describe the evolution of the negative ion density n_-, in this regime.

Consistent with the preceding, the excess electron density within $r<R$ following a *single* laser photodetachment pulse should decay approximately in accordance with

$$n_{e\phi}\cong n_{0+}\frac{e}{kT_e}\phi=-\epsilon J_- n_{0+} \ .$$

The excess electron density therefore turns out to vary as

$$\Delta n_e\equiv[n_e-(1-\epsilon)n_{+0}]$$
$$=\epsilon n_{+0}[1-J_-((R/v_{\text{th}-}t)^2,(r/v_{\text{th}-}t)^2)] \ . \tag{18}$$

The "smeared electron" model which we used, neglecting electron ballistics, is commonly valid in low-frequency phenomena, for ordinary as well as negative-ion plasmas.[10] In our conditions, of course, the ballistic electron term still should play a significant role. The two processes, ballistic and collective, compete against each other, since the field tends to slow down the ballistic outflow of electrons, and the converse. The actual excess electron density Δn_e will decay therefore at a rate *intermediate* between these two extremes, i.e., slower than the very fast ballistic decay $\epsilon n_{+0}(1-J_e)$, but faster than the ion-limited collective decay $\epsilon n_{+0}(1-J_-)$.

VII. DATA INTERPRETATION

We first consider the dominant features of the process and the ordering of time scales. The data (Figs. 3–6) show that the rise time of the density is short in comparison with interspecies collisional times (inverse frequencies) and local creation rates prevailing at the low pressures and densities used here.[1,4,8] Under these conditions, the collision-free Boltzmann (Vlasov) description is indeed appropriate. On the other hand, this time is long (several hundred ns) in comparison with the 7–20-ns transit of electrons at their thermal speed $\approx 3\times 10^7$ cm s^{-1} across the test volume radius R, indicating that the rate-controlling process is the ion inertia, while there is sufficient time for the electrons to come to equilibrium with the self-consistent potential, consistent with our analysis.

A. Dark mode

In this variant, the evolution of n_- is deduced by measuring *differentially* the changes in n_e caused by two laser pulses. This technique has the advantage that it does not involve a fit of the analytic prediction of the n_e decay to the data; as shown above, due to its light mass, both the ballistic and the field-dependent components are important, so that a higher-order analysis would be required. Instead, we use as a measure of $n_-(\Delta t)$ only the instantaneous change in n_e at the start of the search pulse, before a significant evolution of the newly perturbed n_e can take place. The fit of the differential data is therefore directly proportional to n_-, for which we have a good model at early times.

Data fits to the ballistic approximation are illustrated in Figs. 4 and 5, with $R=0.2$ and 0.4 cm, respectively. Both measurements were performed at $r=0$, so that the simplest expression, Eq. (12), can be used to fit the measurements. In Fig. 4 the three values of the parameter R/v_{th-} used in the equation are 2, 2.5, and 3×10^{-7} s, corresponding to $v_{th}\cong10$, 8, and 7×10^5 cm s^{-1}. The data appear to fit best the range $v_{th-}=8\pm1\times10^5$ cm s^{-1}.

From Eq (12) it can be expected that when R is increased, the time evolutions will be slowed down, so that the suitable parameters will be linearly increased. Correspondingly in Fig. 5, with R doubled from 0.2 to 0.4 cm, we increase R/v_{th-} to 4.5, 5.5, and 6.5×10^{-7} s. As seen, this velocity range $v_{th-}\cong9$, 7, and 6×10^5 cm s^{-1} brackets the data points up to 700 ns, the same early time interval as in Fig. 4. The best fit at early times appears to be $v_{th-}=7\times10^5$ cm s^{-1}, overlapping the velocity range in Fig. 4, as expected.

With the larger radius, a longer time interval is required before the process reaches completion. In Fig. 5, the density data now spans a longer time period of 1400 ns, and the rate is seen to decrease after 0.6 μs, indicating that the negative-ion influx slows down at later times. This is consistent with processes neglected in the analysis: collisions and higher-order potential effects. For instance, the inverse of the momentum transfer collision frequency[11] for 0.5-eV electrons in H_2 at 3 mTorr, is about 0.2 μs and the distance between collisions is about 6 cm. These collisions thermalize the excess electrons and thereby affect the evolution of the self-consistent potential, which is no longer simply "driven" by the ion flux, as idealized in Eq. (16). In addition, as will be shown below, the effect of the potential on the ionic densities makes itself felt at just this range of times, so that the lowest-order ballistic ion approximation in the Poisson equation is no longer realisitc. Thus departures from the collisionless (Vlasov) picture are expected, and a more complete solution must be invoked at longer times.

It appears therefore that the ballistic approximation is a reasonable model for the early-time evolution of negative-ion density, and that the rate-determining process is the slow inflow of the relatively heavy negative ions. To maintain charge quasineutrality, that is balanced by an outflow of electrons. The electric field that evolves, though too weak to affect appreciably the ionic motion at early times, is nevertheless effective in coupling the electron motion to the ions because of the much lighter electron mass. Consequently, the electron excess outflow from $r<R$ is retarded and occurs at a speed much reduced below the electron thermal velocity. Because of the physical analogy with ambipolar plasma processes, an appropriate description for such coupled counterflow of oppositely charged species is monopolar transport.

An independent check is provided by comparing probe signal shapes. Figure 6 is a typical plot of electron density decay following a single laser pump pulse (bright mode), together with the negative-ion density increase obtained from two-laser data. A separate trace shows the sum of the two densities. As seen, the time constants of the electron decay and positive-ion increase are comparable, so that there is at first no change in their sum, which approximately equals the positive-ion density, since as shown above the plasma is nearly neutral at early times. Due to the faster electron decay, however, the sum begins to decrease at around 0.6 μs, reaching a minimum at 1.2 μs. This corresponds to a drop of roughly 5% of the negative charge, and an equal increase in the positive charge

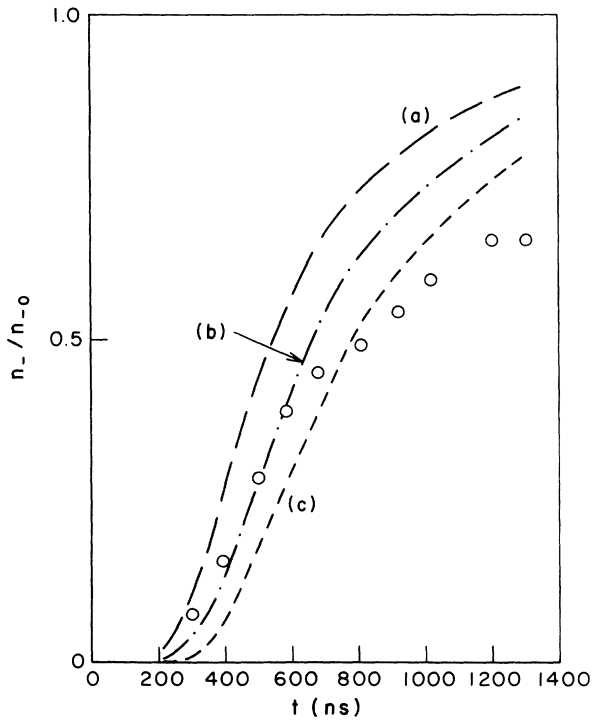

FIG. 5. Recovery of H^- density at $r=0$ for $R=0.4$ cm, and data fits using the ballistic approximation, Eq. (11). Parameter values R/v_{th-} are (a) 4.5×10^{-7} s, (b) 5.5×10^{-7} s, (c) 6.5×10^{-7} s.

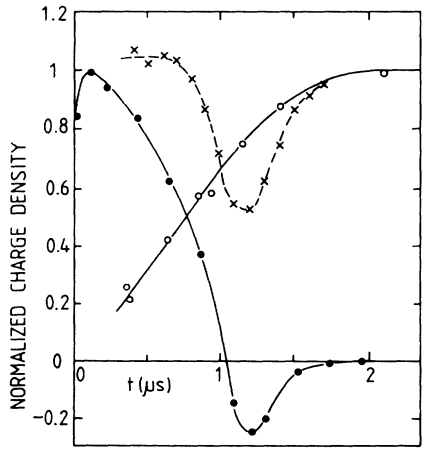

FIG. 6. H^- and electron density recovery, using the bright (●) and dark (○) signal modes at $r=0$. Dashed line: sum of densities.

density. Using simple continuity considerations, one can estimate the density decrease in positive ions due to the field-induced velocity change $\Delta v_+(\phi)$ to be $\Delta n_+ / n_{+0} \approx \Delta v_+ /(R/t)$. For our conditions, using an average mass of 2 for the positive ions, we find $\Delta n_+ / n_0 = 4\%$. In conclusion, both the electron and the positive-ion density behavior are consistent with the limitations due to the approximations used in our analysis.

B. Bright-signal-mode

The bright-signal mode provides a direct method for measuring the reduced, monopolar electron outflow velocity, as well an indirect but independent method for measuring the H^- transport rate. In this mode, one measures the space-time evolution of the photoelectrons created by a single pump pulse, and uses a model of the density evolution to unfold transport properties. The search probe position is scanned from $r=0$ to $r >> R$, and the signal shape is analyzed for nonlocal electron pulses occurring in delayed coincidence with the laser pulse. As pointed out above, this approach requires a fit to the analytical expression for n_e, which is much more field-dependent than n_-. Data obtained in this mode are detailed elsewhere;[12] we discuss here its physical interpretation in terms of our collisionless model.

1. Signal duration at $r=0$

The analysis indicates that at $r=0$, the purely field-dependent component of the excess electron density evolution scales as $(R/v_{\text{th}-}t)$. If one adds a correction c_B for the intial fast ballistic decay to Eq. (18), the actual electron density should have a form

$$\Delta n_e \approx \epsilon n_{+0}(1-J_-) - c_B \ ,$$

where the slow-scale time dependence resides entirely in J_-. The term c_B, due to its fast decay (large v_{the}), is relatively insensitive to R. Consider the point in time at which the normalized excess electron density Δn_e has decreased to zero; i.e., the instant when the probe signal following a single pulse is about to pass through the baseline. It is obtained by solving the preceding equation for the value $t=\tau$ at which $\Delta n_e = 0$. For simplicity, choosing the point $r=0$, this time defined as the "duration" τ is

$$e^{-R^2/(v_{\text{th}}-t)^2} = c_1 \ ,$$

with solution

$$\tau = c_2 \frac{R}{v_{\text{th}-}} \ ,$$

where c_1 and c_2 are constants related to $c_B/\epsilon n_{+0}$. That is, τ should be dominantly linear in R.

This can be verified experimentally. In contrast with the top trace in Fig. 3, which described a typical search signal at $r=0$ for a fixed value of the beam diameter, Fig. 7 presents the effect on signal shape of varying $D=2R$ from 0.1 to 1.2 cm. The major change is the increase in the signal duration τ, the time required for the excess electron density to become depleted. Figure 8 plots τ as a function of $D=2R$ for several gas pressures p. Note that the $\tau - R$ relations are linear, in accordance with the result of our analysis. Further, the duration increases monotonically with p. Since τ is inversely proportional to $v_{\text{th}-}$, this implies that $v_{\text{th}-}$ decreases with p. Independent estimates of H^- drift velocity obtained from H^- current and densities in the extraction region, indicate that the H^- drift velocity decreases with increasing pressure in a similar way.[12,13]

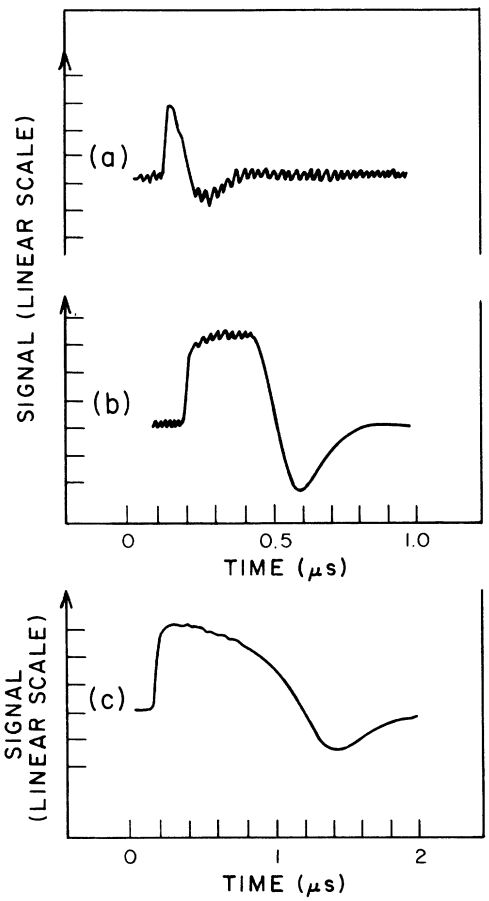

FIG. 7. Single-pulse signal at $r=0$ for various values of laser diameter D. Ordinate: probe electron current, inverted (more light=signal up). (a) Abscissa, 0.1 μs/division; ordinate 0.8 mA/division; $D=0.1$ cm. (b) Abscissa, 0.1 μs/division; ordinate 2 mA/division; $D=0.4$ cm. (c) Abscissa, 0.2 μs/division; ordinate 2 mA/division; $D=1.2$ cm.

2. Signal delay at $r > R$

When the probe is outside the laser beam, $r > R$, a signal shape different from that shown in Fig. 3 is obtained. The signal should correspond to the expected evolution of n_e, Eq. (18); a data fit could be carried out, but it turns out that for $r > R$ the functions J_- are dominated by the factor $(r/v_{\text{th}-}t)$, so that the excess electron density values will propagate approximately as invariants along (r/t).

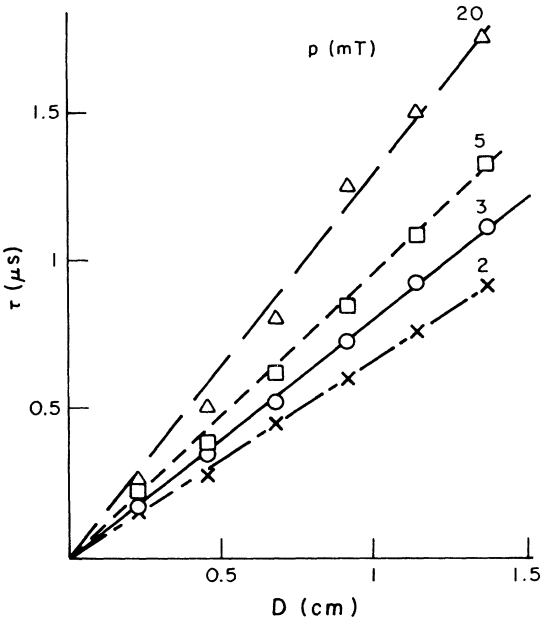

FIG. 8. Dependence of photodetachment pulse duration τ on laser diameter D and pressure p.

Therefore certain overall properties characteristic of self-similar problems are expected, and can be tested for directly.

A simple way to check this is by comparing the dependence of J on (r/t) at values of the ratio (r/R) which are either (i) close to 1, or else (ii) greter than 1, i.e., r sizably beyond R. Note that, *for constant (r/t)*, the ratio (R/t) decreases as r increases. Consider, for instance, a change in t by a factor of 8. In case (i) with $(r/R)=1$, J decreases by nearly 19%; and with $(r/R)=2$, J increases by nearly 18%, over this range of t. That is, when (r/R) is close to unity, J varies appreciably with (r/t). In contrast, for case (ii) with $(r/R)=5$, J increases by only 2.4% over this large range in t (and therefore in R/t), so long as (r/t) remains constant. The physical reason is that, the further r departs from the center, the less effect the size R of the laser beam will have on the propagation of the perturbation, which eventually becomes entirely self-similar in (r/t), with the normalizing coefficient $v_{\text{th}-}$.

This is illustrated below. As shown in Fig. 9, the signal observed when the probe is at some $r > R$ starts off with a small, steep front reaching a plateau, followed by a slower rise to a peak, and a drop-off to its initial level after a total duration τ. We denote by $\Delta\tau$ the delay between the start of the steep front and the peak of the slow rise. The small plateau turns out to be due to prompt photodetachment outside the laser beam, due to reflection of the powerful laser pulse off the bottom of the chamber. This is checked by measuring the dependence of the signal features on decreasing laser intensity. It is found that the prompt plateau at $t < \Delta\tau$ decreases in height as the reflected fraction of laser power dips below saturation, while the major signal features remain invariant, being due to the above-saturation intensity within the laser beam. The delayed peak represents a nonlocal

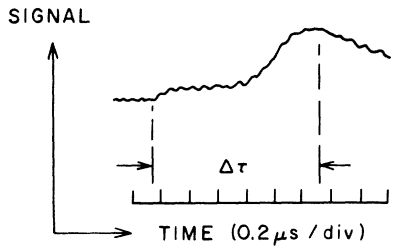

FIG. 9. Typical oscillograms of single-pulse probe current, probe located outside the laser beam $r > R$. Abscissa: time, 0.2 μs/division. Ordinate: probe electron current, 2 mA/division, inverted (more light = signal up).

effect detected at the probe position but originating within the laser beam. It should follow that the delay $\Delta\tau$ will exhibit radial symmetry with respect to the beam center.

This is verified by scanning the probe position along chords traversing the laser beam. Two cases are shown. (i) Figure 10 corresponds to a diametral chord (passing through $r=0$). The delay time is symmetric in the radial coordinate r, and becomes constant as the probe transits from $r > R$ to $r < R$. The width of the saturated zone closely corresponds to the laser beam diameter D, as it should. The slope of the $D - \Delta\tau$ curve for large values of r corresponds to $v_{\text{th}-} = 7\times10^5$ cm s^{-1}, in close agreement with previous values. (ii) In the second case, the probe is scanned along a chord tangent to the laser beam, defining the photodetached volume. As expected, a sharp minimum in the delay is found to occur at the point of closest approach (chordal coordinate x) shown in Fig. 11. The slope starts off with a larger value $v_{\text{th}-} \cong 12\times10^5$ cm s^{-1}, at small values of the chordal coordinate x, as can be expected on geometric grounds, and decreases with increasing x (i.e., as x approaches r) to the same

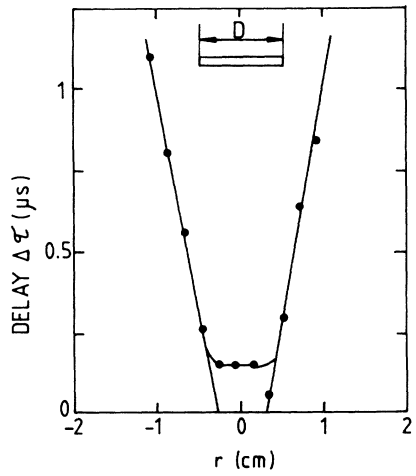

FIG. 10. Variation of delay $\Delta\tau$ with probe position r along diametral chord. Inset shows radial location of laser beam (test volume); D is laser beam diameter.

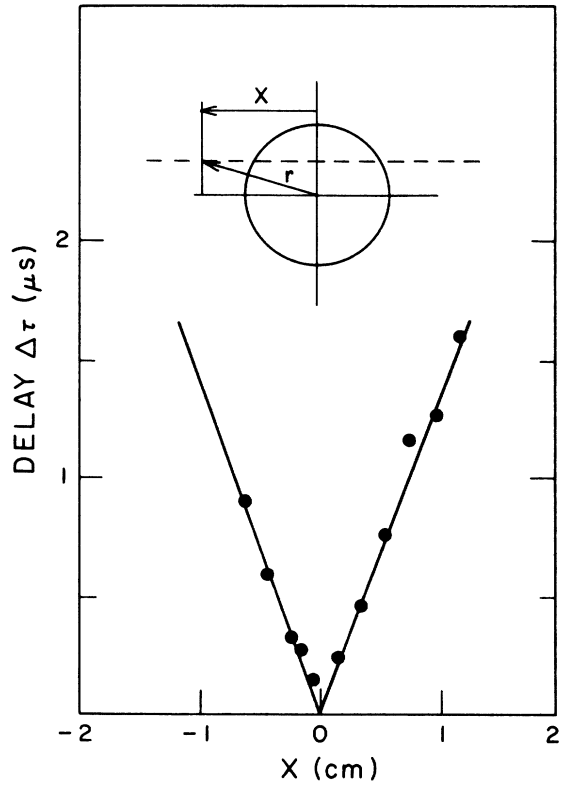

FIG. 11. Variation of delay $\Delta\tau$ with probe position x along chord tangent to $r=R$. Inset shows plan view of laser beam (circular cross section); dashed line illustrates a typical probe chordal (nontangent) trajectory, chordal coordinate axis x, and its relation to radial coordinate r.

values $v_{th-} \cong 7\times10^5 \text{cm s}^{-1}$. The fact that data obtained with the probe located inside and outside the laser beam yields similar values indicates that no significant perturbation of the local H^- temperature is caused by the probe. This could be expected since the probe zone of influence (a few Debye lengths) is negligible in comparison with the test volume dimensions, in these cases.

C. Factors in data reduction

To verify the independence of our model from geometric factors, tests were also conducted in an inverse configuration which still retains cylindrical symmetry. In this geometry, the probe is positioned at the center of the laser beam, $r=0$, but disks of various radii R and centered on $r=0$ are interposed between probe tip and beam, casting a shadow of radius R around the probe. Hence photodetachment occurs only within an annular region surrounding the probe. The signal now is similar to Fig. 9, i.e., exhibits the delay typical of signals obtained with the probe far from the beam axis $r>D/2$, even though the probe is at $r=0$. For instance, with a disk radius of 0.4 cm, the observed delay of 0.6 ms corresponds to a velocity of 7×10^5 cm s^{-1} at $p=3$ mTorr, close to the other tests.

Several sources for departures between model and observations can be identified. As mentioned above, the analysis is exact but has been carried out in the collision-free limit and the approximate solution stopped at a low order in the field, without taking into account field effects on the ionic densities, as exhibited in Fig. 6. In addition, the approximation only takes into account the static screening, and therefore does not predict the dynamic overshoot in the electron density. Our preliminary experiments also reveal several technical factors which should be guarded against. They include (i) finite size and collection radius of the probe (requiring radial integration of the functions J); (ii) angular and radial misalignment between probe tip and laser axis; (iii) inhomogeneity of laser intensity, and (iv) laser reflection from the chamber walls.

VIII. CONCLUSIONS

The preceding analysis and data interpretation indicate the method to be used under other conditions. As shown, a short-time regime can be isolated in which collisional and self-consistent-field effects, including oscillations, have not yet reached sizeable proportions, so that a simple model can be used to fit the data. To describe later times Eq. (16) can be solved, so long as the plasma remains collisionless. For higher densities, when collisions are important, solutions of the diffusion equation for a great variety of conditions are available. The creation rate can also be unfolded from the data in the dark mode, by scanning the search laser beam in space as well as time[14] and varying the beam size D. The expansion of the Boltzmann velocity distribution function in general also has well-known approaches,[15] which may be followed to describe the overshoot[12] and possible oscillations. Note also that these techniques can be used also for measuring H^- properties within the extracted particle beam.

In summary, a kinetic analysis of the dynamic evolution of plasmas subject to a localized central density nonuniformity has been carried out, and the results compared to experimental measurements of density changes following photodetachment laser pulses in plasmas containing H^-. Under our conditions (collisionless, low fraction of H^-), a low-order approximation, linear in the self-consistent potential, fits the observations. Three types of diagnostics: two-pulse ("dark") and one-pulse ("bright") techniques, at $r=0$ and $r>0$, yield comparable data, which are also in rough agreement with drift velocities inferred from extraction experiments. The technique has yielded the first estimates of H^- transport velocities within a volume source, and also demonstrated an unusual type of charged-particle transport in plasmas: a single-charge analog to ambipolar transport.

Based on these results, we conclude that optical tagging, generalized to include nonresonant laser-induced transitions from bound to continuum states, provides a new diagnostic approach applicable to important situations where conventional probe or spectroscopic methods are limited. To start with, systematic measurements of the temperature of H^- in volume sources can now be initiated. In view of the high space and time resolution, the

diagnostic also applies to the local measurement of negative-ion speeds near extraction electrodes, and to beams, in order to achieve better understanding of the balance between extraction speed, density, and beam brightness. More generally, the beam properties of species such as H^- which do not possess accessible bound states can be studied, within complicated geometries, by the method described here and its variants.

ACKNOWLEDGMENTS

We gratefully acknowledge discussions with H. J. Doucet, J. M. Buzzi, E. Zweibel, S. Robertson, and J. Taillet. This work was supported by Direction des Recherches, Etudes et Techniques (France), the Oak Ridge National Laboratory, and North Atlantic Treaty Organization Grant No. RG85/0452. One of us (R.A.S.) acknowledges support under U.S. Army Contract No. DAAG29-81-0-0100, and the National Science Foundation, Grants No. PHY-8312489 and No. PHY-8707338.

APPENDIX

1. Intermediate steps between Eqs. (6) and (7)

The steps intermediate between Eqs. (6) and (7) in the text are Eqs. (A1)–(A10) below.

Equation (6) in the text defines the ballistic density components

$$n_B=\int_{-\infty}^{\infty} d\mathbf{v}[f(\mathbf{v}',\mathbf{r}',t')]|_{t'=0} . \tag{A1}$$

Here $\mathbf{r}'$ is the zeroth-order particle orbit, given by

$$\mathbf{v}=\mathbf{v}', \quad \mathbf{r}'=\mathbf{r}+\mathbf{v}(t'-t) . \tag{A2}$$

Define the variable

$$\mathbf{s}\equiv\mathbf{r}'|_{t'=0}=\mathbf{r}-\mathbf{v}t . \tag{A3}$$

Solving for $\mathbf{v}$, Eq. (A3) yields

$$\mathbf{v}'|_{t'=0}=\mathbf{v}\equiv(\mathbf{r}-\mathbf{s})/t . \tag{A4}$$

Using the definition of $\mathbf{s}$, Eq. (A3), as well as Eq. (A4), $f(\mathbf{v}',\mathbf{r}',t')|_{t'=0}$ the integrand in Eq. (A1) can now be expressed as a function of $\mathbf{s}$,

$$f(\mathbf{v}',\mathbf{r}',t')|_{t'=0}=f(\mathbf{v}'=(\mathbf{r}-\mathbf{s})/t,\mathbf{r}'=\mathbf{s},t'=0) . \tag{A5}$$

Transform the integral $\int d\mathbf{v}$ in Eq. (A1) into an integral $\int d\mathbf{s}$, using the connection between $\mathbf{v}$ and $\mathbf{s}$ given by Eq. (A4). The Jacobian calculated from this equation is $(-t^{-3})$. The new limits of integration corresponding to $\mathbf{v}=\pm\infty$ are $\mathbf{s}/t=\mp\infty$. Using Eq. (A5), Eq. (A1) now becomes

$$\begin{aligned} n_B&=-\int_{\infty}^{-\infty} d\mathbf{s}\, t^{-3} f(\mathbf{v}'=(\mathbf{r}-\mathbf{s})/t,\mathbf{s},t'=0) \\ &=\int_{-\infty}^{\infty} d\mathbf{s}\, t^{-3} f(\mathbf{v}'=(\mathbf{r}-\mathbf{s})/t,\mathbf{s},t'=0) . \end{aligned} \tag{A6}$$

In our instance, f at $t'=0$ has the (separable) form

$$f_0(\mathbf{v})g(\mathbf{s})=\pi^{-3/2}v_{\rm th}^{-3}e^{-\mathbf{v}^2/v_{\rm th}^2}g(\mathbf{s}) , \tag{A7}$$

where f_0 is Maxwellian [Eq. (5)] and $g(\mathbf{s})$ defines the initial density distribution in space, piecewise constant in $\mathbf{s}$.

Use Eq. (A4) to express $\mathbf{v}$ as a function of $\mathbf{s}$ in Eq. (A7), and substitute into Eq. (A6):

$$\begin{aligned} n_B&=\pi^{-3/2}v_{\rm th}^{-3}\int_{-\infty}^{\infty} d\mathbf{s}\, t^{-3}e^{-[(\mathbf{r}-\mathbf{s})/(v_{\rm th}t)]^2}g(\mathbf{s}) \\ &=\pi^{-3/2}v_{\rm th}^{-3}\int_{-\infty}^{\infty}\frac{ds_x}{t}\int_{-\infty}^{\infty}\frac{ds_z}{t}\int_{-\infty}^{\infty}\frac{ds_z}{t}e^{-[(x-s_x)^2+(y-s_y)^2]/(v_{\rm th}t)^2-(z-s_z)^2/(v_{\rm th}+)^2}g(\mathbf{s}) \end{aligned} \tag{A8}$$

in Cartesian coordinates. Transform to polar coordinates defined as follows: $s_{\rm radial}=r'$, $s_{\rm axial}=z'$; $s_x=r'\cos\theta'$, $s_y=r'\sin\theta'$, and $s_z=z'$. Similarly, $x=r\cos\theta$, $y=r\sin\theta$, and $z=z$. The Jacobian of the transformation is $ds_x ds_y ds_z=dr'r'd\theta' dz'$.

In our case, the initial density distribution in space $g(\mathbf{s})$ has the general form (cylindrically symmetric) for all species:

$$g(\mathbf{s})=\begin{cases} n_0, & \text{a constant, for } \mathbf{s} \text{ in the region } R_{\rm min}<s_{\rm radial}<R_{\rm max},\ z_{\rm lower}<s_{\rm axial}<z_{\rm upper} \\ 0, & \text{everywhere else} . \end{cases} \tag{A9}$$

The parameters n_0, $R_{\rm min,max}$, etc., are different for the various species, and described in Sec. VI C in the text.

Substituting Eq. (A9), the integral in Eq. (A8) now yields

$$n_B(r,\theta,z,t)=n_0\pi^{-3/2}v_{\rm th}^{-3}\int d\theta'\int\frac{dr'}{t}(r'/t)e^{-[(r\cos\theta-r'\cos\theta')^2+(r\sin\theta-r'\sin\theta')^2]/(v_{\rm th}t)^2}\int\frac{dz'}{t}e^{-(z-z')^2/(v_{\rm th}t)^2} , \tag{A10}$$

where the integration limits [from Eq. (A9)] are now restricted to the range over which $g(\mathbf{s})$ is nonzero,

$$0<\theta'<2\pi, \quad R_{\rm min}<r'<R_{\rm max}, \quad z_u<z'<z_l .$$

This is Eq. (7) in the text.

2. Intermediate steps between Eqs. (7) and (11)

The steps intermediate between Eqs. (7) and (11) in the text are listed below. Expand the exponent in the integrand of the radial integral in Eq. (7) [Eq. (A10)],

$$(r\cos\theta-r'\cos\theta')^2+(r\sin\theta-r'\sin\theta')^2=r^2+r'^2-2rr'(\cos\theta\cos\theta'+\sin\theta\sin\theta')=r^2+r'^2-2rr'\cos(\theta-\theta') .$$

Introducing this result into Eq. (A10) and inverting the order of integration, one obtains

$$n_B(r,\theta,z,t)=n_0\pi^{-3/2}v_{\rm th}^{-3}e^{-(r/v_{\rm th}t)^2}\int\frac{dr'}{t}(r'/t)e^{-(r'/v_{\rm th}t)^2}\int d\theta' e^{2rr'\cos(\theta-\theta')/(v_{\rm th}t)^2}\int\frac{dz'}{t}e^{-(z-z')^2/(v_{\rm th}t)^2} . \tag{A11}$$

Changing variables from θ' to $\xi=(\theta'-\theta)$, with a corresponding change of limits to $-\theta$ and $(2\pi-\theta)$, the angular integral takes the form

$$\int_{-\theta}^{2\pi-\theta}d\xi\, e^{[2rr'/(v_{\rm th}t)^2]\cos\xi} .$$

Because the exponent in the integrand is periodic (2π), and the integration spans a complete period, it follows that the integral is independent of the parameter θ, which appears in both limits. The integral is then seen to be

$$\int_0^{2\pi}d\xi\, e^{2[rr'/(v_{\rm th}t)^2]\cos\xi}=2\pi I_0(2rr'/(v_{\rm th}t)^2) ,$$

where I_0 is the Bessel function of the first kind of imaginary argument. Introducing this into Eq. (A11) reduces it to

$$n_B(r,z=0,t)=2n_0\pi^{-1/2}e^{-(r/v_{\rm th}t)^2}\int_{R_{\rm min}/v_{\rm th}t}^{R_{\rm max}/v_{\rm th}t}\frac{dr'}{v_{\rm th}t}\frac{r'}{v_{\rm th}t}e^{-(r'/v_{\rm th}t)^2}I_0(2rr'/(v_{\rm th}t)^2)\int_{z_l/v_{\rm th}t}^{z_u/v_{\rm th}t}\frac{dz'}{v_{\rm th}t}e^{-(z-z')^2/(v_{\rm th}t)^2} . \tag{A12}$$

As specified in the text, the dz' integration in our case (large ratios of $|z_{l,u}|$ to $v_{\rm th}t$) reduces to the factor $\pi^{1/2}$. Now Eq. (A12) becomes

$$n_B(r,z=0,t)=2n_0e^{-(r/v_{\rm th}t)^2}\int_{R_{\rm min}/v_{\rm th}t}^{R_{\rm max}/v_{\rm th}t}\frac{dr'}{v_{\rm th}t}e^{-(r'/v_{\rm th}t)^2}I_0(2rr'/(v_{\rm th}t)^2) . \tag{A13}$$

This is Eq. (8) in the text. The function of $J(x,y)$ is defined[9] by

$$1-J(x,y)=2e^{-\rho^2}\int_0^{\beta}te^{-t^2}I_0(2\rho t)dt,\quad x=\beta^2,\ y=\rho^2 .$$

Expressing the integral in Eq. (A13) in terms of J yields

$$n_B(r,z=0,t)/n_0\cong J((R_{\rm min}/v_{\rm th-}t)^2,(r/v_{\rm th}t)^2)-J((R_{\rm max}/v_{\rm th-}t)^2,(r/v_{\rm th}t)^2) . \tag{A14}$$

This is Eq. (10) in the text. For the negative ions, for instance, the range within which the initial density is nonzero is $R_{\rm min}=R$ (laser radius) $<r'<R_{\rm max}$, the chamber radius. If $R_{\rm max}\approx\infty$, then the second term on the rhs above becomes zero, leading to Eq. (11) in the text,

$$n_{B-}(r,z=0,t)/n_0\cong J((R/v_{\rm th-}t)^2,(r/v_{\rm th-}t)^2) .$$

---

[1] J. R. Hiskes, Comments At. Mol. Phys. **19**, 59 (1987).

[2] R. A. Stern, D. N. Hill, and N. Rynn, Phys. Lett. **93A**, 127 (1983); R. A. Stern, Europhys. News **15**, 2 (1984).

[3] M. Bacal and G. W. Hamilton, Phys. Rev. Lett. **42**, 1538 (1979); M. Bacal, A. M. Bruneteau, and M. Nachman, J. Appl. Phys. **95**, 15 (1984).

[4] J. M. Wadehra, Phys. Rev. A **29**, 106 (1984).

[5] R. A. Stern and J. A. Johnson III, Phys. Rev. Lett. **34**, 1584 (1975); R. A. Stern, Phys. Fluids **21**, 1287 (1978). H^- has no single-electron excited state below the detachment limit; hence Doppler techniques using passive or laser-induced fluorescence spectroscopy do not apply directly.

[6] M. W. Siegel, R. J. Celotta, J. L. Hall, J. Levine, and R. A. Bennett, Phys. Rev. A **6**, 607 (1972); R. J. Celotta *et al.*, *ibid.* **6**, 631 (1972); H. Hotop and W. C. Lineberger, J. Phys. Chem. Ref. Data **4**, 539 (1975); for a recent reference, see R. Trainham, G. D. Fletcher, N. B. Mahsour, and D. J. Larson, Phys. Rev. Lett. **59**, 2291 (1987).

[7] M. Bacal, G. W. Hamilton, A. M. Bruneteau, H. J. Doucet, and J. Taillet, Rev. Sci. Instrum. **50**, 719 (1979).

[8] G. Gioumousis and D. P. Stevenson, J. Chem. Phys. **29**, 294 (1958); A. M. Bruneteau and M. Bacal, J. Appl. Phys. **57**, 4342 (1985); M. Bacal, A. M. Bruneteau, H.J. Doucet, G. W. Hamilton, and J. Taillet, Laboratoire de Physique des Milieux Ionises, Ecole Polytechnique, Palaiseau, France, Report No. PMI 896, 1978.

[9] Yudell L. Luke, *Integrals of Bessel Functions* (McGraw-Hill, New York, 1962); S. Goldstein, Proc. R. Soc. London **219**, 151 (1953); **219**, 171 (1953).

[10] See, for instance, S. G. Tagare and R. V. Reddy, Plasma Phys. Controlled Fusion **29**, 671 (1987); the same physical assumptions underlie studies of strongly inhomogeneous classical (electron-positive ion) plasmas, starting with A. V. Gurevich, L. V. Pariiskaya, and L. P. Pitaevskii, Zh. Eksp. Teor. Fiz. **49**,

647 (1965) [Sov. Phys—JETP **22**, 449 (1966)], as well as the Risø group, Ref. 15 below.

[11]A. V. Engelhardt and A. V. Phelps, Phys. Rev. **131**, 2115 (1963).

[12]P. Devynck, J. Auvray, M. Bacal, P. Berlemont, J. Bruneteau, R. Leroy, and R. A. Stern, Rev. Sci. Instrum. **60**, 2873 (1989).

[13]M. Bacal *et al.*, in *Production and Application of Light Negative Ions*, Proceedings of the Second European Workshop, Palaiseau, 1986, edited by M. Bacal (Ecole Polytechnique, Palaiseau, France, 1986), pp. 17 and 201.

[14]J. C. Herper, I. Palocz, N. Axelrod, and R. A. Stern, J. Appl. Phys. **45**, 224 (1974).

[15]P. Michelsen and H. L. Pécseli, Phys. Fluids **16**, 221 (1973).